# A High-Resolution Hyperspectral Imaging System for the Retina

**Minh Ha Tran,[a,b] Michelle Bryarly,[a,b] Kelden Pruitt,[a,b] Ling Ma,[a,b] Baowei Fei [a,b,c*]**

[a] Center for Imaging and Surgical Innovation, University of Texas at Dallas, Richardson, TX
[b] Department of Bioengineering, University of Texas at Dallas, Richardson, TX
[c] Department of Radiology, University of Texas Southwestern Medical Center, Dallas, TX

\* e-mail: bfei@utdallas.edu, Website: www.fei-lab.org

## ABSTRACT

In this study, we developed an imaging system that can acquire and produce high-resolution hyperspectral images of the retina. Our system combines the view from a high-resolution RGB camera and a snapshot hyperspectral camera together. The method is fast and can be constructed into a compact imaging device. We tested our system by imaging a calibrated color chart, biological tissues *ex vivo*, and a phantom of the human retina. By using image pansharpening methods, we were able to produce a high-resolution hyperspectral image. The images from the hyperspectral camera alone have a spatial resolution of 0.2 mm/pixel, whereas the pansharpened images have a spatial resolution of 0.1 mm/pixel, a 2x increase in spatial resolution. Our method has the potential to capture images of the retina rapidly. Our method preserves both the spatial and spectral fidelity, as shown by comparing the original hyperspectral images with the pansharpened images. The high-resolution hyperspectral imaging device can have a variety of applications in retina examinations.

## 1. INTRODUCTION

Historically, the spectral signatures of biological tissues has been used to monitor health and diagnose diseases [1]. Initial efforts in spectral signature acquisition and analysis utilized spectrometers, which were limited to capturing a small spatial region. This limitation was significantly addressed with the advent of hyperspectral imaging (HSI), which integrated spectral and spatial data to create a "hypercube" – a three-dimensional representation of an imaged area. Spectral imaging is more powerful than RGB in various biomedical tasks – such as determining oxygen saturation in blood, diagnosing thyroid cancers with H&E stains, or scanning for early signs of skin cancer [2]. Thanks to advances in engineering, spectral cameras are becoming lightweight, more compact, and more accessible for researchers. As such, in the last two decades, there has been an explosion of research in HSI for the purpose of biomedical diagnosis and monitoring. The majority of diagnosis applications have been used for *in vivo* structures such as the skin, the mouth, and the retina [1-3].

The retina, with its direct connection with the brain through the optic nerve, is considered part of the central nervous system (CNS). Subsequently, it is considered the only part of the CNS that is exposed and can be monitored *in vivo* without any invasive procedure. Many of the diseases of the CNS manifest as biomarkers in the retina, such as multiple sclerosis, Alzheimer's disease (AD), and stroke. To identify these biomarkers, imaging techniques such as optical coherent tomography (OCT) have been used to measure the thickness of the retinal nerve layer [4, 5]. Hyperspectral imaging has the potential to provide a noninvasive alternative. Many of these biomarkers also exhibit changes in the visible light spectrum, changes that can be detected and analyzed with HSI [6, 7]. Spectral imaging were used to monitor diabetic retinopathy and map retinal oxygenation rate [8]. Most notably, hyperspectral imaging has been used to identify Amyloid beta deposit in the retina, one of the early markers of AD [9]. Experiments have been conducted on mouse models and in human clinical trials that show the diagnosis potential of HSI for early screening of AD.

Due to the delicate nature of the retina, it is important that the acquisition time is short, and the illumination used does not exceed a damaging threshold. The limit of white light exposure to the retina should not exceed ~180 μW for 5 seconds or ~120 μW for 30 seconds [10]. Illumination constraints placed a limit on the types of spectral acquisition hardware. There are four main methods of acquiring HS images: spatial scanning ("push broom"), spectral scanning, spatial-spectral scanning, and snapshot. Spatial scanning cameras ("push-broom") typically requires a long acquisition time, which is not

suitable for producing fast images and as such are not commonly seen for retinal imaging applications. Spectral scanning cameras use a system of fast-changing spectral filters to sequentially scan through each spectrum, producing a series of high-resolution images. Many retinal imaging applications use spectral scanning cameras, however their scanning time often last around 1-2 minutes [2]; this can be improved. Snapshot imaging systems, especially those using spectrally resolved detector arrays (SRDA), are capable of acquiring hyperspectral images in real time [2]. SRDA is manufactured by depositing filters in a mosaic manner on top of a CMOS sensor. The resulting image is demosaiced to produce hyperspectral cube. SRDA systems are possible thanks to modern engineering capabilities, and they are being increasingly common in research that involves retinal imaging [11, 12]. Their compact size (less than 100 grams in weight) is also a benefit, because they can be used to construct compact systems [2].

However, there is a downside to these SRDA snapshot imaging cameras. The raster size of the acquired image is small compared to that acquired by push broom cameras. For example, if a SRDA has 16 different wavelengths arranged in a $4 \times 4$ grid, then the final image is 16 times smaller compared to the image taken with the underlying CMOS. In the retina, there are various micro-vascular structures that provide helpful hints toward screening or diagnosis. If the raster size is not large, then the spatial resolution is coarse, and these microstructures might not be visible. To overcome this, we propose a hardware and software solution. In the hardware side, we propose a system that acquire both snapshot hyperspectral image and RGB high resolution images. Our retina acquisition system is based on the topical endoscopy fundus imaging (TEFI) system created by Paques et al [13]. The system is notable because it can achieve high resolution digital images of mice fundus and cost very little. To our knowledge, our proposed method is the first that applies pansharpening and beam-splitter configuration to TEFI. In the software side, we created a workflow to register the two images and merge them together to produce high resolution hyperspectral images. This is the first system of its kind to be used for retinal imaging, and we believe that its real-time acquisition and analysis means that we can acquire high-quality data without harming the eyes.

In the following sections, we first describe the hardware system and how we validated the systems using phantom studies. Then, we described the analysis of the hyperspectral images, and proposed an automatic workflow to produce high-resolution, hyperspectral images using pansharpening algorithms.

## 2. METHOD

### 2.1 Hardware System

We constructed our system by connecting an endoscope with a fixed-focal length lens to provide magnification. Illumination was provided through a fiber optic wire that travels in the same direction as the scope. A simplified diagram of the system is shown in Figure 1a, along with the actual photographs of the system shown in Figure 1b. The scope is connected to a 10-90 beam splitter and diverts the light into an RGB camera and a hyperspectral snapshot camera. This unbalanced division of light is chosen because the HSI camera requires significantly more light compared to the RGB camera due to the number of filters it has. Connecting the cameras with the scopes are fixed-focal length lens. The snapshot camera captures 16 bands of images at raster size of $270 \times 512$ pixels each band in the wavelengths 460 – 600 nm. It acquired hyperspectral images through bandpass Fabry-Perot filters arranged in an alternating pattern [14]. The RGB camera is a standard scientific CMOS camera (ToupTek C3CMOS series) and can acquire images at raster size of up to $3072 \times 2048$ pixels. The illumination is provided by a Xenon lamp (Olympus) through a flexible optic fiber to the endoscope. The entire system is fixed in place vertically, with the scope pointing down toward the imaging subject.

We tested two different types of scopes for the purpose of different applications: a laparoscope and a small industrial borescope. The laparoscope will be used in surgical settings. It has a length of 40.5 cm and a diameter of 0.4 inch (10 mm). The borescope will be used to image the retina of small animals, as well as small vascular structures. It has a length of 80 mm and an outside diameter of 1.65 mm.
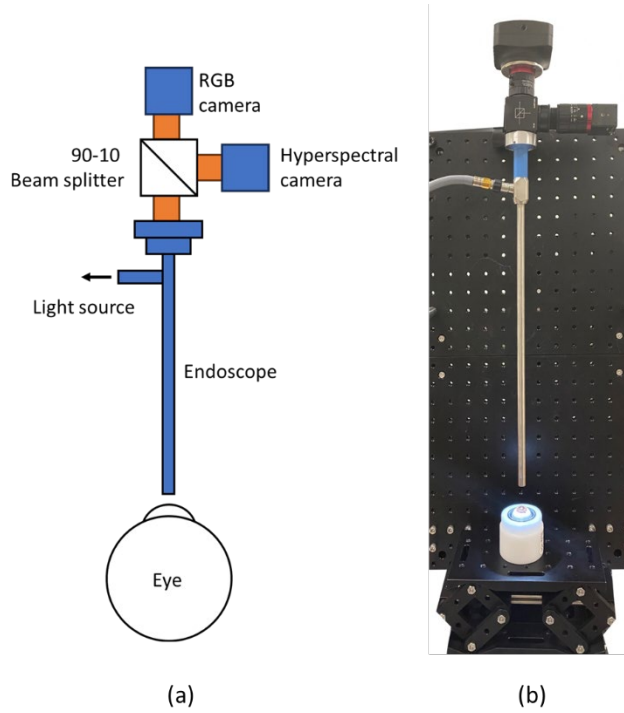
Figure 1. (a) Diagram of the dual-camera hyperspectral RGB system. The system's advantage is that it is compact and can be constructed using off-the-shelf components. (b) An image of the actual system using a laparoscope. Here, we used a phantom model of the human retina as our target.

## 2.2 Image Acquisition and Analysis

We developed a software system that can simultaneously capture hyperspectral image and RGB image at the same time. Subjects were placed on top of a translating platform that can move up and down. The platform is used to move the subjects into focus. Prior to imaging subjects, we acquired dark and white references by using a 95% reflective Spectralon target. The final image is color-corrected using both the white and dark references using the following formula:

$$I = \frac{I_{raw} - I_{dark}}{I_{white} - I_{dark}}$$

In this equation, $I_{raw}$ is the raw acquired image. $I_{dark}$ is the dark reference, $I_{white}$ is the white reference image, and $I$ is the final corrected image. The raw image is a mosaiced image, so we used our demosaicing method to produce final hyperspectral images [15]. The raster resolution of an RGB image is $3072 \times 2048 \times 3$ pixels, and the raster resolution of a hyperspectral image is $512 \times 270 \times 16$ pixels.

## 2.3 Generation of High-resolution Images

To produce high-resolution images, we created an automatic imaging workflow. The workflow has three stages: pre-processing, registration, and pansharpening. For preprocessing, separate pipelines were proposed for RGB images and hyperspectral images. The RGB image was converted to grayscale. For the hyperspectral images, because there were noises within the images, we decided to apply a $3 \times 3$ median filter to each individual channels before registration. We registered the grayscale, high resolution images and the hyperspectral images using the SURF registration method [16]. Registration was performed in MATLAB (Mathworks R2023a) image processing toolbox with the assumption of similarity transformation (only rotation, translation, and scaling applied). The high-resolution image was rescaled to a spatial dimension of $1024 \times 540$ pixels, which is four times the raster size of the hyperspectral image.

We tested several different methods for image pansharpening. Because pansharpening is a well-studied problem in remote sensing, we relied on published methods and applied them to our application. The methods we tested were: Brovey

transformation [17], coupled-nonnegative matrix factorization [18], guided fusion PCA [19], Gram-Schmidt transformation [20], intensity-hue transformation [21], PanNet [22], smoothing filter-based intensity modulation [23]. The methods were implemented in Python [24]. The final image has a spatial dimension of $1020 \times 540 \times 16$ pixels, which is 4 times the raster size of the original hyperspectral image.

## 2.4 Tissue and Phantom Studies

We demonstrated the system viability in a variety of spectral and biological targets. The first target imaged was a colored chart (Calbrite, ColorChecker Passport 2) that contains 24 colors. The color chart was used to assess the accuracy of our system in preserving spectral fidelity. The color chart measures $125 \times 90\ mm$ in dimension. In addition to the 24 colored square, the target also contains marked lines that are 1 mm apart. We used marked lines to assess the spatial quality of the imaging system. We imaged the color chart under Halogen light, with an exposure time of 5 seconds.

To simulate biological tissues in clinical situations, we imaged heart tissues of pig *ex vivo.* We cut out a section of the ventricle to photograph. The tissue was roughly square shaped and measured 1 centimeter on each side. We imaged the pig heart tissue under Xenon light, with an exposure time of 5 seconds.

To simulate retinal imaging in clinical situations, we used a model phantom of the human retina (Ocular Instrument, OEM-7). The model phantom included simulated blood vessels that have diameters of less than 100 microns. The pupil of the phantom retina has a 7 mm diameter, which is roughly equal to the diameter of our laparoscope. We imaged the retina under Xenon light, provided through a fiber optic cable. Figure 1b shows the setup that was used to image the retina. Prior to imaging, we used a light meter to measure the illumination power of the Xenon light. The Xenon light should have a low illumination power so that they can be applicable for clinical retinal imaging. The tip of the endoscope was placed less than 1 mm away from the surface of the object. The exposure time was 5 seconds and did not exceed the recommended maximum laser exposure power of ~180 µW [10].

## 2.5 Metrics

We employed two metrics to compare different pansharpening techniques. The goal is to ensure that the pansharpened, high resolution image preserves both the spectral fidelity (compared to the hyperspectral image captured by the snapshot camera) and the spatial fidelity (compared to the RGB image captured by the CMOS camera). As such, we use two different metrics. To measure spectral fidelity, we use root mean square error (RMSE). We first down-sample the pansharpened image into the same dimension as the original, median filtered hyperspectral image. RMSE is minimized when there is a similarity in the spectral profile:

$$RMSE = \sqrt{\frac{\sum_{all\ channels}\sum_{all\ pixels}(i_{PAN}-i_{HSI})^2}{\sum_{all\ channels}\sum_{all\ pixels}1}} \tag{1}$$

To measure spatial fidelity, we use structurally similarity index measure (SSIM). SSIM can be a good metric for measuring the spatial similarities between two images. It relies on the measurements of the variances and the covariances between two images of similar sizes. If $\mu_x, \sigma_x, \sigma_{xy}$ are the mean and variance of image $x$, and the covariances between images $x$ and $y$, respectively, then the formula for SSIM is given as:

$$SSIM(x,y) = \frac{(2\mu_x\mu_y+c_1)(2\sigma_{xy}+c_2)}{(\mu_x^2+\mu_y^2+c_1)(\sigma_x^2+\sigma_y^2+c_2)} \tag{2}$$

In this formula, $c_1$ and $c_2$ are stabilizing variables. We compared the SSIM for each channel with the high-resolution RGB images, then averaged the SSIM scores with equal weights given to every channel.

## 3. RESULT

### 3.1 Quantitative Results

Here, we compare the quantitative results between different pansharpening algorithms with the purpose of identifying the algorithm of choice. As seen, the method of smoothing filter-based intensity modulation (SFIM) and guided fusion PCA (GFPCA) produces the best RMSE and SSIM scores compared to other methods. However, when looking at the actual

pansharpened images, we see that the images produced by GFPCA are very blurry and is not up to the spatial quality that we expect. Therefore, we continued our investigation using the SFIM method.

Table 1. Comparison between three pansharpening methods that we tested on different imaging subjects. RMSE and SSIM scores are multiplied by 100.

| Method | Color chart | | Pig's heart | | Retina | |
|--------|-------|--------|-------|--------|--------|--------|
| | RMSE | SSIM | RMSE | SSIM | RMSE | SSIM |
| **BV** | 6.170 | 91.921 | 6.148 | 78.838 | 6.170 | 91.921 |
| **CNMF** | 3.114 | 89.956 | 3.472 | 75.563 | 4.579 | 77.444 |
| **GFPCA** | **0.993** | 82.118 | 1.165 | **65.835** | 0.533 | 74.056 |
| **GS** | 5.541 | 88.113 | 6.246 | 86.586 | 7.032 | 80.488 |
| **IHS** | 5.539 | 88.809 | 6.249 | 86.416 | 7.146 | 80.138 |
| **SFIM** | 0.995 | **78.657** | **0.530** | 66.323 | **0.309** | **72.877** |
| **PanNet** | 3.164 | 85.752 | 6.534 | 86.474 | 15.851 | 75.805 |

**BV: Brovey, CNMF: coupled-nonnegative matrix factorization, GFPCA: guided fusion PCA, GS: Gram-Schmidt transformation, IHS: intensity-hue transformation, SFIM: smoothing filter-based intensity modulation. Bolded shows the best performance.**

## 3.2 Qualitative Results

Figure 2 shows the side-by-side comparison of the original hyperspectral image (Figures 2a and 2b) and the pansharpened image (Figures 2c and 2d) of the colored target at the 9th band. We compared both the visual details and the spectral details in the pansharpened image. Visual inspection shows that the pansharpened image improved the spatial quality, as seen in the legible ruler markings on the right side of the images. Each line is spaced 1 mm apart. In the original hyperspectral image, it is not possible to resolve between each marking. We estimated a spatial resolution of around 1 mm/pixel in the original image. In the pansharpened image, the line markings are clearly resolved. Using Michelson contrast measurement [25], we measured a spatial resolution of 0.5 mm/pixel, twice that of the original. We took squared sections from the hyperspectral image and the pansharpened image and compared their spectral profiles. The result was shown in Figure 3. The spectral fidelity was well preserved.
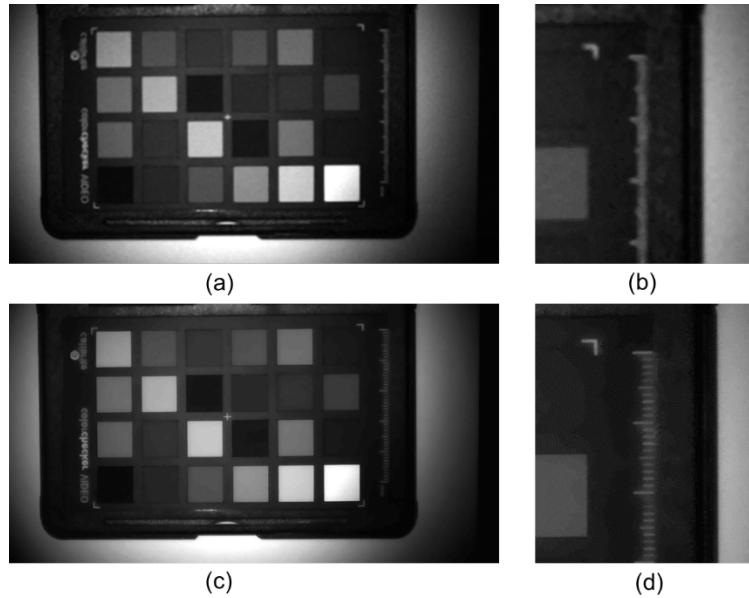
Figure 2. Result of pansharpening applied to a color chart. The images shown were taken from the 9th frame of the hyperspectral cube. Notice the ruler is more resolved on the lower image. The distance between each mark corresponds to 1 mm.
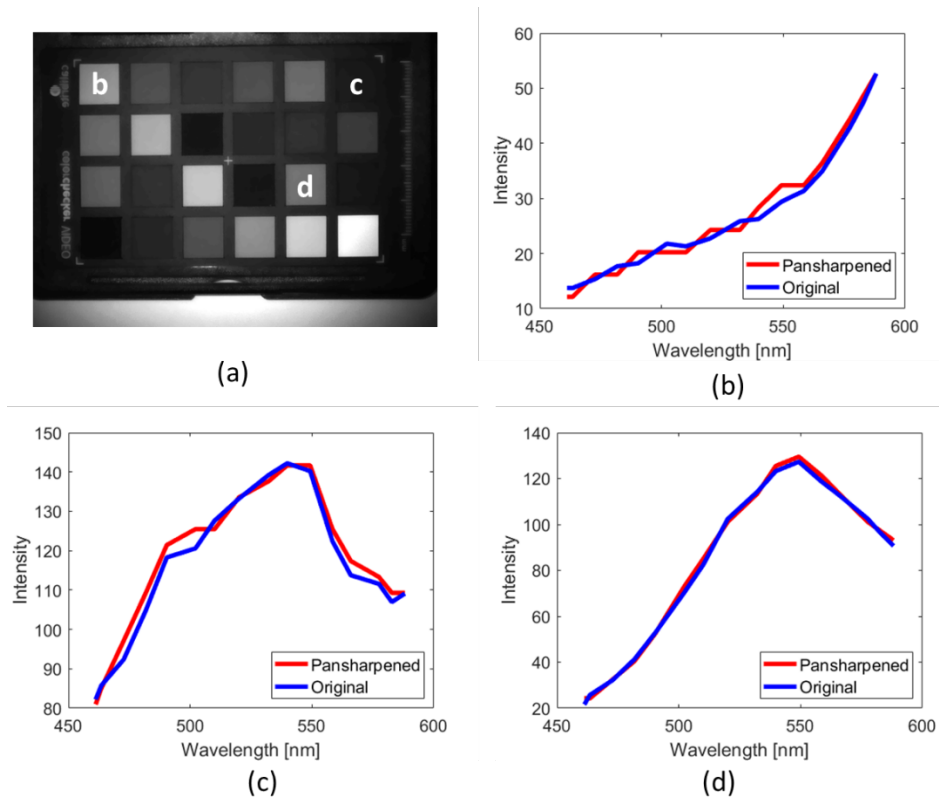


Figure 3. Comparison of spectral fidelity between the pansharpened image and the hyperspectral image at three samples point. (b), (c), and (d) show the comparison of pansharpened spectra (red) and hyperspectral spectra (blue) in the corresponding points marked b, c, and d in Figure (a).

Figure 4 shows the comparison of the original hyperspectral image (Figure 4a and 4b) and the pansharpened hyperspectral image (Figure 4c and 4d) of heart tissues of pig. Visual inspection shows the pansharpened image improves the spatial quality compared to the original hyperspectral image. The section photographed shows a section of the cardiac muscle and a section of fat tissue. In the original image, while the tissues photographed can be identified, the details of the tissue morphology are only seen in the pansharpened image. In the detail section, we zoomed in on a section of the cardiac tissue. In the pansharpened image, the musculature of the ventricle is shown in improved details over that of the original hyperspectral image. By measuring the physical distances between known points in the actual tissue, we calculated the spatial resolution of the original hyperspectral image to be around 0.2 mm/pixel, whereas the spatial resolution of the pansharpened image to be around 0.1 mm/pixel.

Figure 5 shows side-by-side comparison of the original hyperspectral image (Figures 5a and 5b) and the pansharpened hyperspectral image (Figures 5c and 5d) of the phantom retina. Visual inspection shows that the pansharpened image resolves the retinal vessels with higher details that are not seen in the hyperspectral image. This is promising news, considering that this model contains vessels with diameter equal to that in the human retina. By measuring the physical distances between known points in the phantom retina, we calculated the spatial resolution of the original hyperspectral image to be around 0.2 mm/pixel, whereas the spatial resolution of the pansharpened image to be around 0.1 mm/pixel. Figure 6 compares the mean spectra in the region of interests (ROI) highlighted. This ROI contains a section of the blood vessels. Figure 6b shows that the pansharpened image preserved the spectral signature of blood vessels. This means that the pansharpened image can potentially be used to estimate different biosignature of the retinal blood vessels.
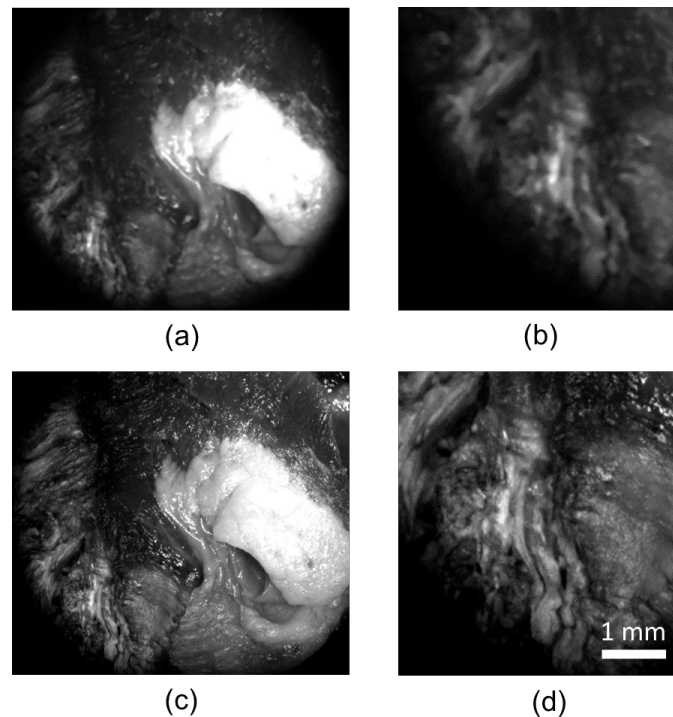


(a)  (b)

(c)  (d)

Figure 4. Result of pan-sharpening applied to an image of pig's heart *ex vivo*. The images shown were taken from the 9th frame of the hyperspectral cube. (a) Original hyperspectral image taken from the snapshot camera. (b) Details of Figure (a). (c) Pansharpened image. (d) Details of Figure (c).
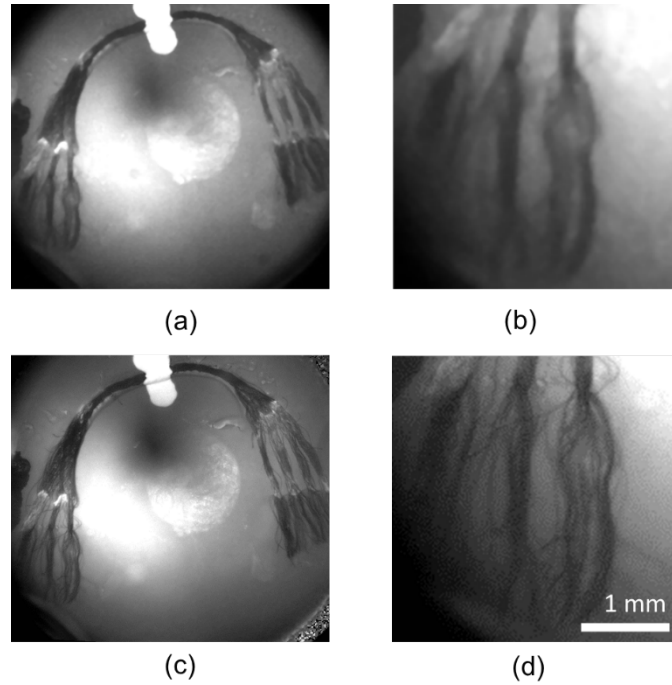
Figure 5. The result of pan-sharpening applied to an image of our model retina. The images shown were taken from the 9th frame of the hyperspectral cube. (a) Original hyperspectral image taken from the snapshot camera. (b) Details of Figure (a). (c) Pansharpened image. (d) Details of Figure (c).
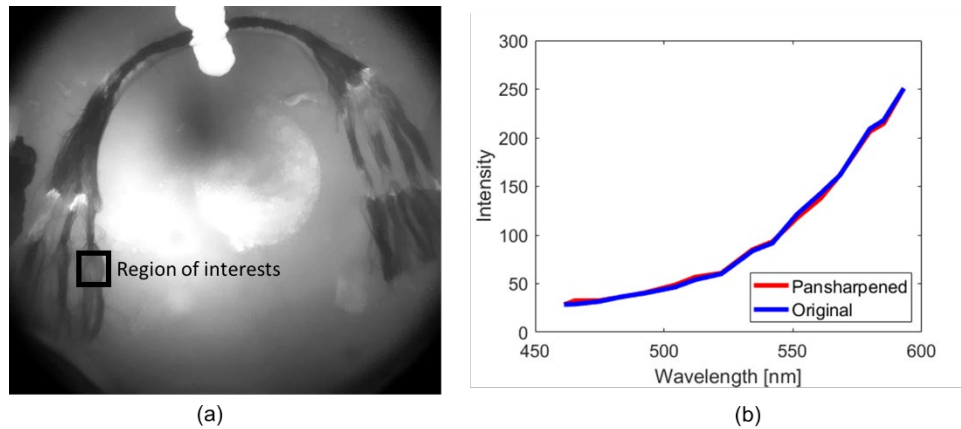


Figure 6. (a) Selection of region of interests, which shows a phantom blood vessel in the phantom retina. (b) Comparison of spectra inside the region of interest between the image taken by the hyperspectral camera (blue), and the pansharpened image (red).

## 4. DISCUSSION AND CONCLUSION

We developed a compact high-resolution hyperspectral imaging system for the retina. The system combines the speed of a snapshot hyperspectral camera with the spatial resolution of an RGB camera. The enhanced spatial resolution provided by our hybrid imaging system is important for the detection and monitoring of eye conditions such as diabetic retinopathy and early signs of Alzheimer's disease. Furthermore, the hyperspectral imaging system could measure oxygen saturation in the retina, a critical factor in diagnosing various ocular conditions. Our system was thoroughly tested on a calibrated

color chart, a model phantom of the eye, and on biological tissues. Further testing and validation on human and animal subjects are needed to determine the clinical relevance of our system. Future work will focus on the image analysis and quantification tools that will help streamline the registration and merge processes to enhance user-friendliness and enable more widespread use. Our proposed system represents a significant advancement in retinal imaging technology, offering real-time acquisition of high-resolution hyperspectral images. Further research and development are needed to fully realize its application potential.

## 5. ACKNOWLEDGEMENTS

## REFERENCES

[1]     G. Lu and B. Fei, "Medical hyperspectral imaging: a review," *Journal of Biomedical Optics,* vol. 19, no. 1, p. 010901, 2014.  Available: https://doi.org/10.1117/1.JBO.19.1.010901.

[2]     M. H. Tran and B. Fei, "Compact and ultracompact spectral imagers: technology and applications in biomedical imaging," *Journal of Biomedical Optics,* vol. 28, no. 4, p. 040901, 2023.  Available: https://doi.org/10.1117/1.JBO.28.4.040901.

[3]     L. Ma and B. Fei, "Comprehensive review of surgical microscopes: technology development and medical applications," *J. Biomed. Opt.,* vol. 26, no. 1, p. 010901, 2021.  Available: https://doi.org/10.1117/1.JBO.26.1.010901.

[4]     F. A. Medeiros *et al.*, "Detection of Glaucoma Progression with Stratus OCT Retinal Nerve Fiber Layer, Optic Nerve Head, and Macular Thickness Measurements," *Investigative Ophthalmology & Visual Science,* vol. 50, no. 12, pp. 5741-5748, 2009, doi: 10.1167/iovs.09-3715.

[5]     D. L. Budenz *et al.*, "Determinants of Normal Retinal Nerve Fiber Layer Thickness Measured by Stratus OCT," *Ophthalmology,* vol. 114, no. 6, pp. 1046-1052, 2007/06/01/ 2007, doi: https://doi.org/10.1016/j.ophtha.2006.08.046.

[6]     S. Lemmens *et al.*, "Hyperspectral imaging and the retina: worth the wave?," *Translational vision science & technology,* vol. 9, no. 9, pp. 9-9, 2020.

[7]     E. R. Reshef, J. B. Miller, and D. G. Vavvas, "Hyperspectral Imaging of the Retina: A Review," *Int Ophthalmol Clin,* vol. 60, no. 1, 2020.

[8]     J. G. Dwight, C. Y. Weng, R. E. Coffee, M. E. Pawlowski, and T. S. Tkaczyk, "Hyperspectral Image Mapping Spectrometry for Retinal Oximetry Measurements in Four Diseased Eyes," (in eng), *Int Ophthalmol Clin,* vol. 56, no. 4, pp. 25-38, 2016 2016, doi: 10.1097/iio.0000000000000139.

[9]     X. Hadoux *et al.*, "Non-invasive in vivo hyperspectral imaging of the retina for potential biomarker use in Alzheimer's disease," *Nature Communications,* vol. 10, no. 1, p. 4227, 2019/09/17 2019, doi: 10.1038/s41467-019-12242-1.

[10]    S. Rees and G. Dobre, *Maximum permissible exposure of the retina in the human eye in optical coherence tomography systems using a confocal scanning laser ophthalmoscopy platform* (Fifth International Conference on Lasers in Medicine). SPIE, 2014.

[11]    S. Lemmens *et al.*, "Combination of snapshot hyperspectral retinal imaging and optical coherence tomography to identify Alzheimer's disease patients," *Alzheimer's Research & Therapy,* vol. 12, no. 1, p. 144, 2020/11/10 2020, doi: 10.1186/s13195-020-00715-1.

[12]    H. Li, W. Liu, B. Dong, J. V. Kaluzny, A. A. Fawzi, and H. F. Zhang, "Snapshot hyperspectral retinal imaging using compact spectral resolving detector array," *Journal of Biophotonics,* vol. 10, no. 6-7, pp. 830-839, 2017/06/01 2017, doi: https://doi.org/10.1002/jbio.201600053.

[13]    M. Paques *et al.*, "Panretinal, High-Resolution Color Photography of the Mouse Fundus," *Investigative Ophthalmology & Visual Science,* vol. 48, no. 6, pp. 2769-2774, 2007, doi: 10.1167/iovs.06-1099.

[14] B. Geelen, N. Tack, and A. Lambrechts, *A compact snapshot multispectral imager with a monolithically integrated per-pixel filter mosaic* (SPIE MOEMS-MEMS). SPIE, 2014.

[15] K. Pruitt, B. Johnson, J. Gahan, L. Ma, and B. Fei, "A high-speed hyperspectral laparoscopic imaging system," in *Medical Imaging 2023: Image-Guided Procedures, Robotic Interventions, and Modeling*, 2023, vol. 12466: SPIE, pp. 49-61.

[16] H. Bay, T. Tuytelaars, and L. Van Gool, "Surf: Speeded up robust features," in *Computer Vision–ECCV 2006: 9th European Conference on Computer Vision, Graz, Austria, May 7-13, 2006. Proceedings, Part I 9*, 2006: Springer, pp. 404-417, doi: https://doi.org/10.1007/11744023_32.

[17] T.-M. Tu, S.-C. Su, H.-C. Shyu, and P. S. Huang, "A new look at IHS-like image fusion methods," *Information Fusion,* vol. 2, no. 3, pp. 177-186, 2001/09/01/ 2001, doi: https://doi.org/10.1016/S1566-2535(01)00036-7.

[18] N. Yokoya, T. Yairi, and A. Iwasaki, "Coupled Nonnegative Matrix Factorization Unmixing for Hyperspectral and Multispectral Data Fusion," *IEEE Transactions on Geoscience and Remote Sensing,* vol. 50, no. 2, pp. 528-537, 2012, doi: 10.1109/TGRS.2011.2161320.

[19] W. Liao *et al.*, "Two-stage fusion of thermal hyperspectral and visible RGB image by PCA and guided filter," in *2015 7th Workshop on Hyperspectral Image and Signal Processing: Evolution in Remote Sensing (WHISPERS)*, 2-5 June 2015 2015, pp. 1-4, doi: 10.1109/WHISPERS.2015.8075405.

[20] C. A. Laben and B. V. Brower, "Process for enhancing the spatial resolution of multispectral imagery using pan-sharpening," ed: Google Patents, 2000.

[21] W. Carper, T. Lillesand, and R. Kiefer, "The use of intensity-hue-saturation transformations for merging SPOT panchromatic and multispectral image data," *Photogrammetric Engineering and remote sensing,* vol. 56, no. 4, pp. 459-467, 1990.

[22] J. Yang, X. Fu, Y. Hu, Y. Huang, X. Ding, and J. Paisley, "PanNet: A deep network architecture for pan-sharpening," in *Proceedings of the IEEE international conference on computer vision*, 2017, pp. 5449-5457.

[23] J. Liu, "Smoothing filter-based intensity modulation: A spectral preserve image fusion technique for improving spatial details," *International Journal of remote sensing,* vol. 21, no. 18, pp. 3461-3472, 2000.

[24] A. Guo. "Py_pansharpening." Github. https://github.com/codegaj/py_pansharpening (accessed 01/09/2024, 2024).

[25] H. Kukkonen, J. Rovamo, K. Tiippana, and R. Näsänen, "Michelson contrast, RMS contrast and energy of various spatial stimuli at threshold," *Vision Research,* vol. 33, no. 10, pp. 1431-1436, 1993/07/01/ 1993, doi: https://doi.org/10.1016/0042-6989(93)90049-3.